COMMUNICATION

ADVANCED
SCIENCE
Open Access

Check for
updates

www.advancedscience.com

Anomalously Suppressed Thermal Conduction by Electron-Phonon Coupling in Charge-Density-Wave Tantalum Disulfide

Huili Liu, Chao Yang, Bin Wei, Lei Jin, Ahmet Alatas, Ayman Said, Sefaattin Tongay, Fan Yang, Ali Javey, Jiawang Hong,* and Junqiao Wu*

Charge and thermal transport in a crystal is carried by free electrons and phonons (quantized lattice vibration), the two most fundamental quasiparticles. Above the Debye temperature of the crystal, phonon-mediated thermal conductivity (κ_L) is typically limited by mutual scattering of phonons, which results in κ_L decreasing with inverse temperature, whereas free electrons play a negligible role in κ_L. Here, an unusual case in charge-density-wave tantalum disulfide (1T-TaS$_2$) is reported, in which κ_L is limited instead by phonon scattering with free electrons, resulting in a temperature-independent κ_L. In this system, the conventional phonon–phonon scattering is alleviated by its uniquely structured phonon dispersions, while unusually strong electron-phonon (e-ph) coupling arises from its Fermi surface strongly nested at wavevectors in which phonons exhibit Kohn anomalies. The unusual temperature dependence of thermal conduction is found as a consequence of these effects. The finding reveals new physics of thermal conduction, offers a unique platform to probe e-ph interactions, and provides potential ways to control heat flow in materials with free charge carriers. The temperature-independent thermal conductivity may also find thermal management application as a special thermal interface material between two systems when the heat conduction between them needs to be maintained at a constant level.

Interactions between free electrons and lattice vibration (phonons) in metallic conductors lead to their electrical conductivity decreasing with temperature, an effect that is widely observed and well understood.[1,2] However, effects of electron-phonon (e-ph) interaction on materials' thermal conductivity are not understood as well, and have been experimentally elusive.[3,4] In electrical conductors, in addition to directly conducting heat themselves (contributing to thermal conductivity with the electronic part, κ_e), free charge carriers also couple with and scatter phonons, hence reducing κ_L. The reduction in κ_L arising from e-ph coupling is typically weak as a very high density ($> \approx 10^{20}$ cm^{-3}) of electrons is needed;[4] hence in nonmetallic systems where carrier density is lower, it is hard to be experimentally detected. In metallic systems with very high charge carrier densities, the e-ph scattering could rise to levels that considerably reduce κ_L, but the measured total thermal conductivity $\kappa = \kappa_e + \kappa_L$ would then be dominated by the contribution of κ_e instead. Experimental exploration of the effects of e-ph scattering on thermal

Dr. H. Liu, L. Jin, Prof. A. Javey, Prof. J. Wu
Materials Sciences Division
Lawrence Berkeley National Laboratory
Berkeley, CA 94720, USA
E-mail: wuj@berkeley.edu
Dr. H. Liu, L. Jin, Prof. J. Wu
Department of Materials Science and Engineering
University of California
Berkeley, CA 94720, USA

Dr. C. Yang, B. Wei, Prof. J. Hong
School of Aerospace Engineering
Beijing Institute of Technology
Beijing 100081, China
E-mail: hongjw@bit.edu.cn
Dr. A. Alatas, Dr. A. Said
Advanced Photon Source
Argonne National Laboratory
Lemont, IL 60439, USA
Prof. S. Tongay
School for Engineering of Matter, Transport, and Energy
Arizona State University
Tempe, AZ 85287, USA
Prof. F. Yang
Department of Mechanical Engineering
Stevens Institute of Technology
Hoboken, NJ 07030, USA
Prof. A. Javey
Department of Electrical Engineering and Computer Science
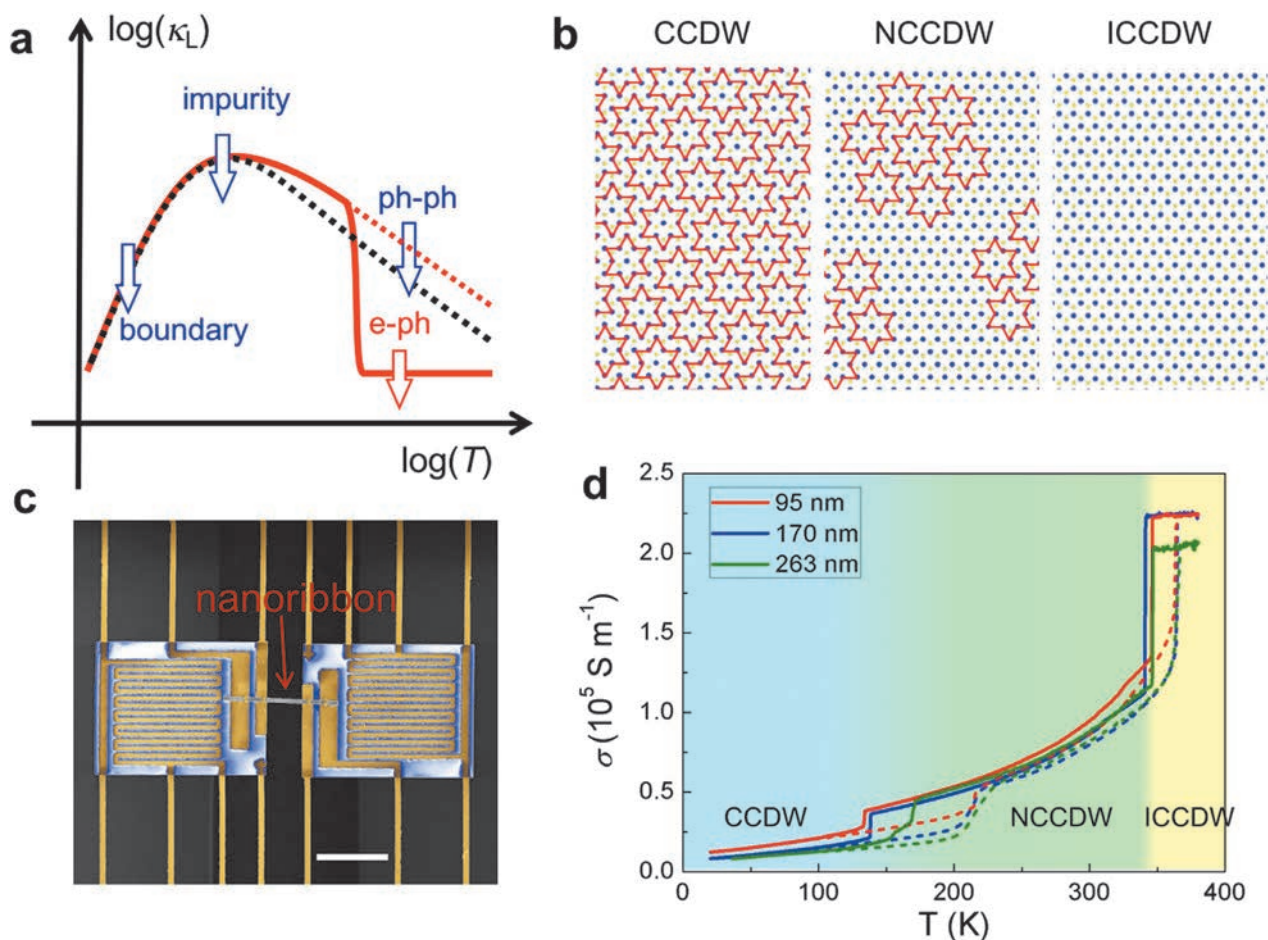University of California
Berkeley, CA 94720, USA

Figure 1. CDW in 1T-TaS$_2$ and nanoribbon devices for electrical and thermal measurements. a) The effect compared to conventional cases: in conventional materials (black dashed line) at high temperatures, lattice thermal conductivity (κ_L) is limited by ph-ph scattering resulting in an $1/T$ dependence, while the effect of e-ph scattering is negligible; the opposite is observed in this work, where ph-ph scattering is intrinsically weak (red dashed line) while e-ph scattering dominantly limits the thermal conductivity, leading to T-independent κ_L (solid red line). Major phonon scattering mechanisms at low (boundary) and intermediate (impurity) temperatures are also indicated. b) Schematic charge-density-wave structures with different levels of commensuration (commensurate as CCDW, nearly commensurate as NCCDW, incommensurate as ICCDW). Red "David stars" represent displacement patterns of Ta atoms. c) False-color SEM image of two suspended pads bridged with a TaS$_2$ nanoribbon that is FIB-bonded onto the underlying Pt electrodes. Scale bar: 20 µm. d) Temperature dependence of electrical conductivity of TaS$_2$ nanoribbons with different thicknesses measured with a four-probe geometry. Solid lines are for cooling and dashed lines are for warming.

transport has been limited to metallic systems at very low temperatures[5] because of the difficulty in separating κ_L from κ_e.

Indeed, recently Liao et al.[4] calculated that κ_L of silicon can be reduced by up to ≈45% in the presence of a high density (≈10^{21} cm^{-3}) of free charge carriers. It has also been proposed that e-ph coupling may be responsible for unusually low values of κ observed in VN$_x$.[6] Yang et al. reported κ_L reduced in NbSe$_3$ nanowires beyond conventional phonon scattering mechanisms that is attributed to e-ph coupling.[7] Theoretical calculations done by Li et al. show that group-V transition metal carbides (VC, NbC, and TaC) host intrinsically strong e-ph coupling and weak ph-ph scattering, leading to κ_L theoretically much lower than the case when the e-ph coupling is absent.[8] As schematically shown in **Figure 1**a, we discover direct experimental evidence of κ_L dominated by e-ph scattering rather than the conven-

tional ph-ph scattering, in a charge-density-wave material, tantalum disulfide (TaS$_2$).

As a layered material, the octahedral (1T) polytype of TaS$_2$ features a well-known series of charge density wave (CDW) phase transitions.[9–11] Above ≈550 K, it takes the normal, metallic phase with the space group of $P\bar{3}m1$. At lower temperatures, CDW phases show up with distinct commensurations with the underlying lattice: an incommensurate (ICCDW) phase above ≈350 K, a nearly commensurate (NCCDW) phase between ≈150 and ≈350 K, and a commensurate (CCDW) phase below ≈150 K. As schematically shown in Figure 1b, in the CCDW phase, the CDW distortion of atoms forms "David-stars" resulting in an ordered $\sqrt{13} \times \sqrt{13}$ superlattice structure. The CDW deformation induces a sizeable energy gap in the electronic band structure.[12] In the NCCDW phase, domains of David-star clusters are isolated from each other by a metallic network, where
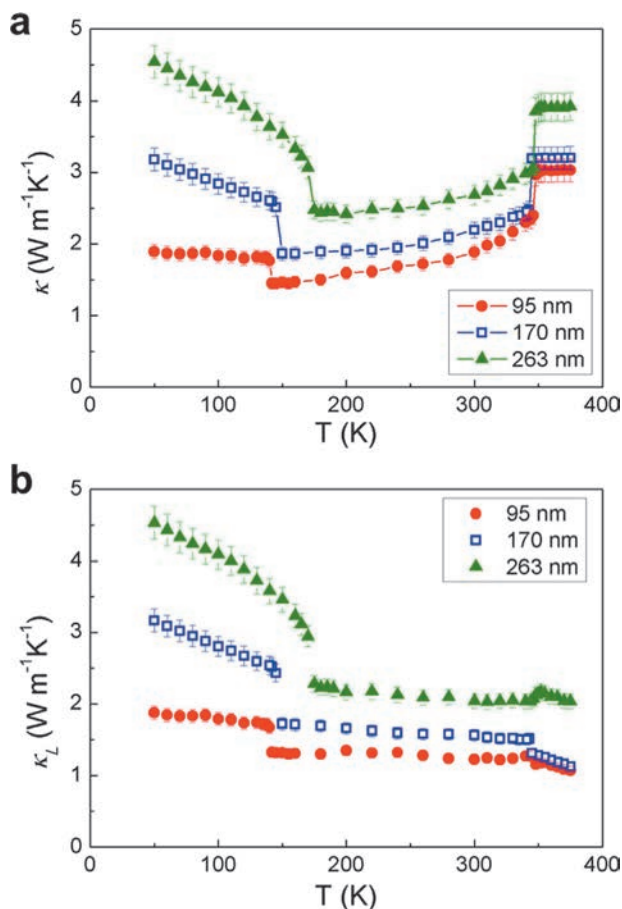
Figure 2. Measured thermal conductivity of TaS$_2$ nanoribbons. a) T dependence of total thermal conductivity (κ) of nanoribbons with different thicknesses. b) Lattice thermal conductivity (κ_L) calculated by subtracting the electron contribution (κ_e) from κ assuming the Wiedemann–Franz law.

electrons behave itinerant. The CDW phases in 1T-TaS$_2$ are correlated with the lattice deformation and simultaneously a Fermi surface instability,[13] where electrons and phonons are strongly coupled to shape its physical properties.

Figure 1c shows the image of a device for electrical and thermal measurements. 1T-TaS$_2$ nanoribbons were fabricated from microflakes mechanically exfoliated out of bulk crystals and measured following the method published previously[14,15] (see details in Experimental Section). Electrical conductivity (σ) of nanoribbons with different thicknesses is shown in Figure 1d. The three phases (CCDW, NCCDW, and ICCDW) are clearly separated in conductivity at the transition temperature of ≈150 and ≈350 K, respectively, with a hysteresis at each transition. Experimentally, it has been reported in bulk 1T-TaS$_2$ samples that the CCDW phase is a semiconductor and the NCCDW phase is effectively a semimetal,[16] and their carrier density is on the order of ≈1 × 10^{19} and ≈1 × 10^{22} cm^{-3}, respectively.[17]

Figure 2a shows measured κ over all three phases, qualitatively consistent with that of bulk samples.[18,19] In addition to a clear overall reduction of κ with nanoribbon thickness, abrupt jumps at each of the phase transition temperature are evident.

To extract κ_L, we calculate κ_e using Wiedemann–Franz law ($\kappa_e = L\sigma T$), where the Lorenz ratio L takes the Sommerfeld value of $L_0 \equiv 2.44 \times 10^{-8}$ W Ω K^{-2}, and subtract κ_e out of the measured κ. The obtained κ_L is shown in Figure 2b. A significant reduction in κ_L between the CCDW and NCCDW phases is observed at the phase transition temperature around 150 K. More interestingly, in the entire NCCDW phase between ≈150 and ≈350 K, κ_L becomes nearly T-independent. Since the Debye temperature of 1T-TaS$_2$ is about 172 K,[20] in the NCCDW temperature range, κ_L is expected to be limited by momentum-nonconserving ph-ph scattering (the Umklapp process), which would result in an $1/T$ dependence as depicted in Figure 1a (black dashed line). The T independence of κ_L, therefore, suggests unconventional phonon scattering mechanisms dominating the Umklapp process in this material.

To suppress the ph-ph scattering, specific phonon dispersions are required to limit the scattering phase space.[8] Due to the lack of long-range order of the lattice structure in the NCCDW and ICCDW phases, we examine phonon dispersions of the normal phase from the first-principles calculation (see details in Experimental Section), to provide insights to the NCCDW phase under investigation. Indeed, recent results from angular-resolved photoelectron spectroscopy shows electronic band structure of NCCDW phase largely in agreement with first-principles calculations based on the normal phase.[16] As shown later, the phonon dispersions we calculated for the normal phase (**Figure 3**a) are also in good agreement with inelastic X-ray scattering (IXS) measurements of the NCCDW phase. Two general features are clearly seen in Figure 3a: (1) the acoustic-optical (a-o) phonon gap is unusually wide, nearly equal to the bandwidth of the acoustic phonons, similar to the case of BAs[21–24] and NbC;[8] and (2) the acoustic phonon dispersions are tightly bunched together. The effect (1) of wide phonon gap is attributed to the large mass ratio in TaS$_2$ ($m_{Ta}/m_S \approx 5.7$),[25] as Ta and S are responsible mostly for the acoustic and optical modes, respectively (Figure 3a). Such an a-o bandgap wider than the maximal acoustic phonon energy prohibits the phonon scattering process that involves two acoustic and one optical phonons (the so-called *aao* process).[21] The effect (2) of acoustic phonon bunching significantly limits the phonon scattering process involving three acoustic phonons (the *aaa* process) by reducing the scattering phase space.[21] As a result, the Umklapp process of ph-ph scattering is greatly suppressed, making room for thermal phonons to be dominantly scattered by other T-independent mechanisms.

To understand phonon properties in the NCCDW phase, we measured the acoustic phonon dispersions using IXS (see details in Experimental Section). The phonon dispersions measured at 300 K along Γ-M and Γ-K directions are shown in Figure 3b with the underlying calculated dispersions (solid line). It can be seen that these transverse acoustic (TA) and longitudinal acoustic (LA) phonon dispersions are indeed bunched together as shown from density functional theory (DFT) calculation. Secondly, Kohn anomalies[26] are observed in the dispersions. For example, along the Γ-M direction, the LA phonon shows phonon softening at wavevector $q_1 \approx 0.6\ q_{Γ\text{-}M}$, consistent with neutron scattering measurements.[27] Along the Γ-K direction, the TA phonon modes also show broad, flat regions at certain range of wavevectors denoted as q_2. Interestingly, these less-dispersive modes generally show larger linewidths (Γ) than
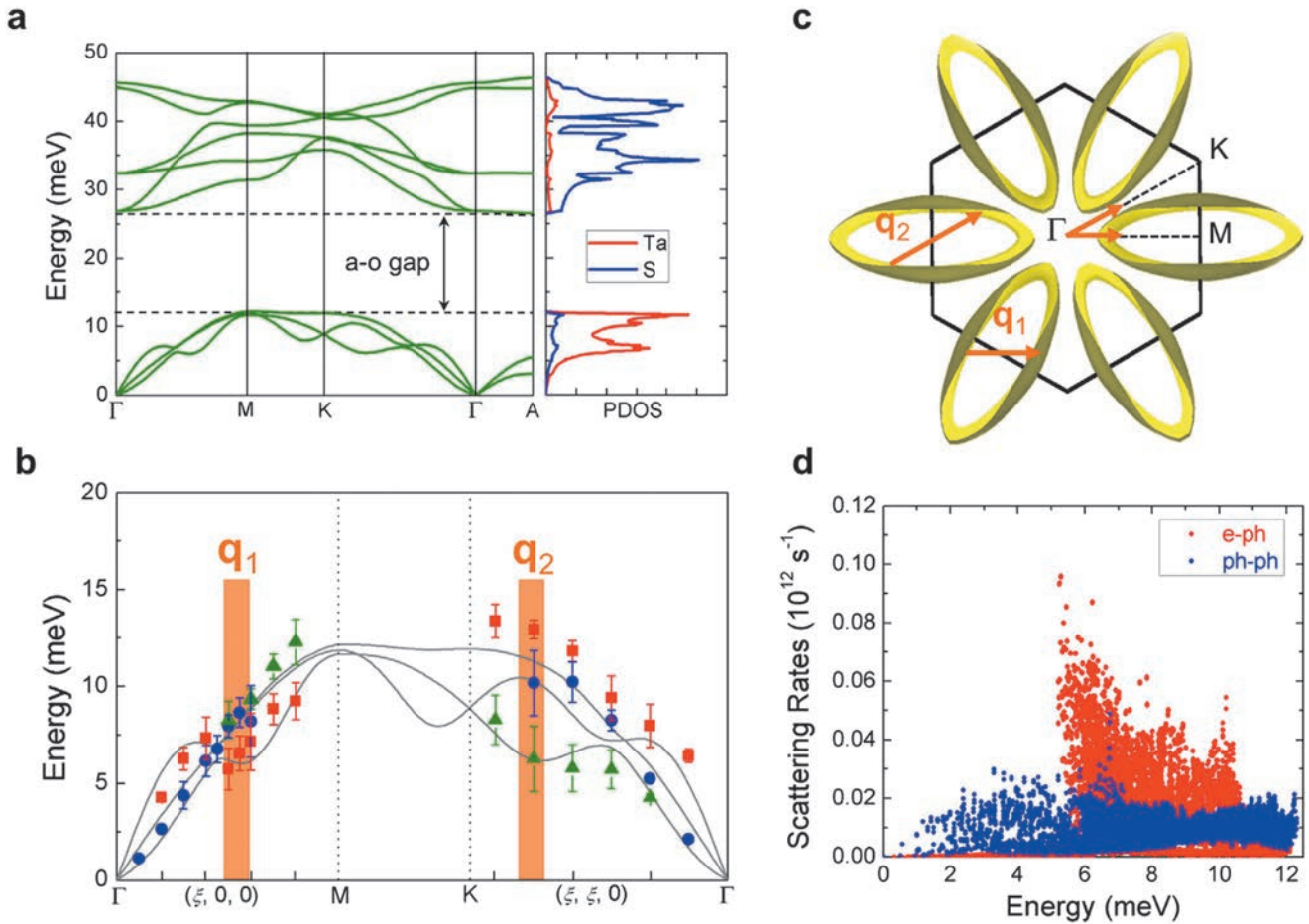
Figure 3. Phonon dispersion and Fermi surface featuring weak ph-ph scattering and strong e-ph coupling. a) Phonon dispersion of the normal phase from DFT calculations, and partial PDOS of $1T$-TaS_2 involving vibration of Ta and S atoms, respectively. The large a-o phonon gap and bunched acoustic phonons suppress ph-ph scattering. A high PDOS peak is seen between 6 and 8 meV, corresponding to the less-dispersive phonon modes. b) Acoustic phonon dispersion (points) of the NCCDW phase measured at 300 K by IXS, overlaid onto the calculated dispersion (solid lines) in (a). The measured phonon linewidth is represented by the error bars. The phonon anomalies along the Γ-M and Γ-K directions are clearly seen, where the linewidth is unusually broadened. c) Calculated electron Fermi surface of $1T$-TaS_2 in the normal phase, which is nested with the two wavevectors q_1 and q_2 along the Γ-M and Γ-K directions, respectively. These two wavevectors are correlated to the phonon anomalies shown in (b), enabling strong e-ph coupling. d) Calculated e-ph (red points) and ph-ph (blue points) scattering rates as a function of phonon energy, showing e-ph scattering rates higher than ph-ph rates for phonon modes between ≈6 and 8 meV.

dispersive modes at comparable energies, as shown in Figure S5, Supporting Information. Since the phonon linewidth is related to phonon scattering rate ($1/\tau$) via the uncertainty principle, $\Gamma \propto 1/\tau$, the experimental data in Figure 3b indicate that the acoustic phonons are unusually strongly scattered near those wavevectors.

To elucidate the mechanism of the momentum-selective phonon scattering, we calculated the Fermi surface of electrons in TaS_2, which is shown in Figure 3c and Figure S6, Supporting Information. On the Fermi surface, there exist regions with large areas that are parallel to each other; hence, it is strongly nested with certain fixed wavevectors q. The nesting allows free electrons to be strongly scattered on the Fermi surface if a momentum $\hbar q$ is externally provided by phonons. Interestingly, the shape of the Fermi surface in Figure 3c features two nesting wavevectors along the Γ-M and Γ-K directions, respectively, quantitatively consistent with the anomaly wavevectors (q_1 and q_2) observed in the phonon dispersions in Figure 3b. This agreement is a proof of

strong coupling between free electrons and acoustic phonons. The e-ph scattering rate for the phonon mode j with wavevector q is given by[1,8]

$$\frac{1}{\tau_{e-ph}} \propto \sum_{mn} \int d\mathbf{k} \left| g_{nm,j}^{e-ph}(\mathbf{k}, \mathbf{q}) \right|^2 \left[f_0(\varepsilon_{nk}) - f_0(\varepsilon_{mk+q}) \right]$$

$$\times \delta\left(\varepsilon_{mk+q} - \varepsilon_{nk} - \hbar\omega_{jq}\right) \quad (1)$$

where ε_{nk} and ε_{mk+q} are electron energies in the initial (n, $\mathbf{k}$) and the final (m, $\mathbf{k}+\mathbf{q}$) states, $\hbar\omega_{jq}$ is energy of the phonon in the state (j, $\mathbf{q}$), f_0 is Fermi distribution, $g_{nm,j}^{e-ph}(\mathbf{k}, \mathbf{q})$ is e-ph scattering matrix element, and the sums are over the electron bands n and m. When the Fermi surface is nested with a wavevector q, phonon modes with momentum $\hbar q$ and energy $\hbar\omega_{jq}$ will be strongly scattered due to the large phase space available in the integration. This is the case for phonon modes near the Kohn anomaly wavevectors

**ADVANCED
SCIENCE NEWS**

www.advancedsciencenews.com

**ADVANCED
SCIENCE**
Open Access

www.advancedscience.com

q_1 and q_2, which are relatively less dispersive and contribute a high phonon density of states (PDOS) between ≈6 and 8 meV (Figure 3a). Acoustic phonon modes at other wavevectors, especially those with smaller wavevectors, experience much weaker scattering rates. This is experimentally evidenced from the very narrow linewidths for phonon modes near the Γ point observed in IXS experiments (Figure 3b). Indeed, as shown in Figure 3d, first-principles calculations confirm that the e-ph scattering rates are considerably stronger than ph-ph scattering rates for acoustic phonon modes of energy higher than 5 meV, especially those between 6 and 8 meV, corresponding to the less dispersive modes near q_1 and q_2.

The unusual temperature-independent thermal conductivity results fundamentally from a nested Fermi surface interplaying with uniquely structured phonon dispersions. These conditions could be met in metallic compounds with large cation/anion mass ratios and signatures of strong e-ph coupling such as superconductivity and CDWs. As high density of charge carriers can be introduced by a gate field via either electrostatics or field-induced insulator to metal transition,[11,28] the effect also reveals a potential way to electrically and locally tune thermal conduction of solids for nonlinear thermal devices.[29,30] New exotic physics of 1T-TaS$_2$, such as quantum spin liquid state,[31] may also need to be invoked as possible additional heat carriers. We also note the complication that in the case of very strong e-ph coupling, a complete separation between lattice and electronic thermal conductivity may not always be possible.[32] We further state that the honeycomb domain walls network of topological excitations in NCCDW phase identified recently[33] may provide new phonon modes for heat conduction in 1T-TaS$_2$.

Experimental Section

1T-TaS$_2$ Nanoribbons Device Fabrication: 1T-TaS$_2$ flakes were mechanically exfoliated onto a SiO$_2$/Si substrate using polydimethylsiloxane, and then nanoribbons (1–2 μm in width and 25–40 μm in length) were produced using electron-beam lithography (EBL) followed by reactive ion etching.[15,34] The flakes were spin coated by poly(methyl methacrylate) (PMMA, C4-950, 4000 rpm) and baked at 180 °C for 5 min. The PMMA was patterned with EBL, followed by a developing process using methyl isobutyl ketone/isopropyl alcohol (IPA) = 1:3 for 1 min. The exposed TaS$_2$ was etched via reactive ion etching using a mixed gas (90% SF$_6$ and 10% O$_2$, 60 sccm) for several seconds. After the PMMA removal with acetone and rinsing by isopropyl alcohol, TaS$_2$ nanoribbons were obtained. Four Ti/Au electrodes were then deposited onto the nanoribbons. To achieve that, a second EBL process was used to expose the electrode areas on the nanoribbons. The exposed areas were Ar$^+$ milled (30–60 s) to remove any oxidized or insulating layer on the surface, and then coated with Ti (10 nm, deposition rate ≈0.5 Å s^{-1}) and Au (70 nm, deposition rate ≈1 Å s^{-1}) metals using electron beam evaporation (CHA Solution E-beam evaporator). A lift-off process was performed in acetone for ≈5 min with gentle shaking, followed by thorough rinsing with IPA. After that, the selected individual TaS$_2$ nanoribbon was manually picked up using a sharp tungsten needle (600 nm tip diameter, Cascade Microtech) in a micromanipulator probe station, and transferred onto an empty, suspended-pad microdevice, aligning the four Ti/Au metal electrodes of the nanoribbon onto the four Pt electrodes on the suspended pads. A small amount of Pt was then deposited along the edge of the predeposited Ti/Au electrodes, to bond them onto the underlying Pt electrodes using a focused ion beam (FIB) (dual-beam FEI Quanta). Such two-step contact formation ensures both good ohmic electrical conduction and negligible thermal resistance of the contacts, while minimizing exposure time to the FIB and the resul-

tant sample damage. Figure S1, Supporting Information, shows schematically the fabrication process and images of a nanoribbon device. The thickness of the nanoribbon was confirmed by atomic force microscopy (AFM) as shown in Figure S1b, Supporting Information. A scanning electron microscopy (SEM) image of the device is shown in Figure 1c. After Pt deposition, electrical quality of the electrodes was verified by a linear *I–V* relationship (ohmic contact), as shown in Figure S2a, Supporting Information. The devices were annealed at 373 K for 1 h in vacuum chamber to further improve electrical and thermal contacts at the electrodes.

Electrical and Thermal Properties Measurements: The electrical resistance and thermal conductance of nanoribbons were measured using suspended-pad microdevices. Such suspended nanoribbon configuration not only maximally relieves substrate-imposed strain and trapped-charge influence, but also ensures that, unlike typical thin film measurements, the electrical and heat fluxes flow along the same path during the measurements. Two SiN$_x$ pads with Pt electrodes were suspended from the Si substrate by long (≈400 μm) and flexural SiN$_x$ arms. Pt serpentine electrodes were patterned on the pads to serve as microheater and thermometer. Four additional Pt line electrodes were deposited for four-probe electrical resistance measurements of the nanoribbon sample. Applying a DC current ($I = 0$–15 μA) to the microheater on one pad, the temperature on it (hot pad) was raised by ΔT_h. The heat flowed through the nanoribbon to the other pad (cold pad) and raised its temperature by ΔT_s. The base temperature of the two pads (global temperature) was controlled with an external heater (Lakeshore 335 temperature controller) and cryogenic compressor cooler (HC-4A, Sumitomo Cryogenics). All the measurements were performed under high vacuum (<10^{-6} Torr) in the vacuum chamber. An AC current with a small amplitude ≈500 nA and frequency ≈1.1 kHz (199 Hz) was applied to the Pt serpentine electrodes to probe ΔT_h (ΔT_s) on the hot (cold) pad using lock-in amplifiers on the basis of the temperature coefficient of resistance of Pt electrodes. The temperature coefficient of resistance of the Pt electrodes at individual temperatures over the temperature range of measurements was calibrated. The thermal conductance of the nanoribbon (G) is given by $G = (P \times \Delta T_c)/(\Delta T_h^2 - \Delta T_c^2)$,[14,35] where P is the heating power of a microheater, $P = I^2 \times (R_h + R_{arm})$, and R_h and R_{arm} are the resistance of Pt electrode on the heating pad and suspended arm, respectively. Electrical resistance of the nanoribbon was measured by the four-probe method using a Keithley nanovoltmeter (2182A) and precision current source (6220). The dimensions of nanoribbons were determined from both SEM and AFM. Data errors were estimated from errors in size of the nanoribbon and ΔT_h and ΔT_c on the pads: ≈8% for thermal conductivity and ≈5% for electrical conductivity.[14,15,36] Thermal contact resistance of the devices is negligible as shown in Figure S2b, Supporting Information.

Inelastic X-Ray Scattering Measurements: Phonon dispersions of single crystal 1T-TaS$_2$ were measured using IXS technique. Specifically, phonon dispersion branches along the Γ-M and Γ-K directions were measured using the HERIX X-ray spectrometer at beamline 30-ID-C at the Advanced Photon Source using 23.7 keV ($\lambda = 0.5226$ Å) X-rays with a focused beam spot size of ≈30 μm.[37] The 1T-TaS$_2$ single crystal sample was a large bulk flake with a lateral size of 2–3 mm and thickness of 50–100 μm, as shown in Figure S3, Supporting Information. The thickness was selected to obtain the maximum scattering signal in transmission IXS measurements. The flake was adhered onto a copper rod using thermally conductive epoxy, and the rod was then mounted on an evacuated heating stage for rotation in a vacuum chamber. During the measurement, the counting time was in the range of 30–60 s for each energy scan at a constant Q. The measured energy spectra were fitted using a Gaussian function for the elastic peak and a damped harmonic oscillator function for the phonon peaks.[38,39] Figure 3b presents the experimental IXS results, where the phonon energy, $E = \hbar\omega$, is plotted versus the magnitude of the wavevector (q) along the Γ-M and Γ-K directions in the reciprocal space. Scattering geometry was used to determine the specific polarization of the atomic vibration for these phonon branches. The scattering vector, Q, is defined by the summation of a Bragg peak position and a small vector as $Q = G + q$, where G is the reciprocal lattice vector, and q is a wavevector in the 1st Brillouin zone. Therefore, the phonon branches were measured from combinations of Q and q with different Bragg peak positions, and the longitudinal and TA

polarizations of phonons were measured separately.[40,41] As an example for the phonon branch along Γ-K direction, the LA phonon dispersion was measured at reciprocal-lattice points $Q_{LA} = (1 + \xi, 1 + \xi, 0)$ with $\xi = 0.05$–0.3, and the TA phonon dispersion was measured at $Q_{TA} = (\xi, \xi, 4)$. Q_{LA} and Q_{TA} are the total scattering vectors, and $q = (\xi, \xi, 0)$ is the measured phonon wavevectors. In the schematic reciprocal space with $\xi = 0.15$ as shown in Figure S4a (in Supporting Information), the phonon wavevector of $q = (0.15, 0.15, 0)$ is parallel to Q_{LA} and approximately perpendicular to Q_{TA}, which reveals the longitudinal and transverse atomic vibrations with respect to the phonon propagation direction, respectively. Figure S4b, Supporting Information, shows a plot of the experimental energy scan at $Q_{TA} = (0.15, 0.15, 4)$ of the TA branch. The phonon linewidths were extracted from this line shape function convoluted with experimental resolution function. Figure S5, Supporting Information, illustrates the phonon linewidth for dispersive and less dispersive phonon modes in the NCCDW phase of 1T-TaS$_2$ at 300 K, where the less dispersive phonon modes show more phonon linewidth broadening than the dispersive modes at comparable energies.

Simulation Methods: First-principles calculations were performed in the framework of DFT as implemented in the Quantum Espresso (QE) package[42,43] with a plane-wave cutoff of 55 Ry. The DFT calculations were carried out using norm-conserving pseudopotentials[44] to describe the electron-ion interaction in the local density approximation of the exchange-correlation interaction. The van der Waals correction was considered with the method of dispersion correction of DFT (DFT-D3).[45] The fully relaxed lattice constants of $a = 3.350$ Å and $c = 5.954$ Å (experimental values:[46] $a = 3.367$ Å, $c = 5.902$ Å) were obtained. The 3D Fermi surface structure was simulated with the WANNIER90 code[47] and visualized with the XCrySDen package.[48] An electronic smearing of 0.05 Ry was applied in the calculation to stabilize the system and prevent it from undergoing the CDW transition.[49,50] The phonon-electron scattering rates were calculated using the EPW (e-ph coupling using Wannier functions) code[51–53] within the QE package[42,43] following the procedure described by Li et al.[8] The phonon dispersions and e-ph matrix elements were calculated within density functional perturbation theory as implemented in QE on a coarse 9 × 9 × 5 q grids and electron band structure on a 18 × 18 × 10 k grid. The coarse grid quantities were interpolated to fine k and q grids of 45 × 45 × 21 within the EPW package. The phonon-phonon scattering rates were calculated using the D3Q package within the QE.[54–56]

Supporting Information

Supporting Information is available from the Wiley Online Library or from the author.

Acknowledgements

Conflict of Interest

The authors declare no conflict of interest.

Author Contributions

H.L. and C.Y. contributed equally to this work. J.W. conceived the project. H.L. and J.W. designed the experiments. H.L. fabricated devices and performed the thermal and electrical measurements. H.L., B.W., A.A., A.S., and J.H. performed the inelastic X-ray scattering measurements. C.Y. and J.H. performed the theoretical calculation. S.T. grew the single crystal flake of sample. H.L., C.Y., B.W., L.J., F.Y., J.H., and J.W. discussed the data. H.L. and J.W. wrote the draft. All authors contributed to discussing the data and editing the manuscript.

[1] J. M. Ziman, *Electrons and Phonons: The Theory of Transport Phenomena in Solids*, Oxford University Press, Oxford **2001**.

[2] N. W. Ashcroft, N. D. Mermin, *Solid State Physics*, Holt, Rinehart and Winston, New York **1976**.

[3] F. Giustino, *Rev. Mod. Phys.* **2017**, *89*, 015003.

[4] B. Liao, B. Qiu, J. Zhou, S. Huberman, K. Esfarjani, G. Chen, *Phys. Rev. Lett.* **2015**, *114*, 115901.

[5] W. H. Butler, R. K. Williams, *Phys. Rev. B* **1978**, *18*, 6483.

[6] Q. Zheng, A. B. Mei, M. Tuteja, D. G. Sangiovanni, L. Hultman, I. Petrov, J. E. Greene, D. G. Cahill, *Phys. Rev. Mater.* **2017**, *1*, 065002.

[7] L. Yang, Y. Tao, J. Liu, C. Liu, Q. Zhang, M. Akter, Y. Zhao, T. T. Xu, Y. Xu, Z. Mao, Y. Chen, D. Li, *Nano Lett.* **2019**, *19*, 415.

[8] C. Li, N. K. Ravichandran, L. Lindsay, D. Broido, *Phys. Rev. Lett.* **2018**, *121*, 175901.

[9] B. Sipos, A. F. Kusmartseva, A. Akrap, H. Berger, L. Forró, E. Tutiš, *Nat. Mater.* **2008**, *7*, 960.

[10] M. Eichberger, H. Schafer, M. Krumova, M. Beyer, J. Demsar, H. Berger, G. Moriena, G. Sciaini, R. J. D. Miller, *Nature* **2010**, *468*, 799.

[11] Y. Yu, F. Yang, X. F. Lu, Y. J. Yan, Y.-H. Cho, L. Ma, X. Niu, S. Kim, Y.-W. Son, D. Feng, S. Li, S.-W. Cheong, X. H. Chen, Y. Zhang, *Nat. Nanotechnol.* **2015**, *10*, 270.

[12] K. Rossnagel, N. V. Smith, *Phys. Rev. B* **2006**, *73*, 073106.

[13] F. Clerc, C. Battaglia, M. Bovet, L. Despont, C. Monney, H. Cercellier, M. G. Garnier, P. Aebi, H. Berger, L. Forró, *Phys. Rev. B* **2006**, *74*, 155114.

[14] L. Shi, D. Li, C. Yu, W. Jang, D. Kim, Z. Yao, P. Kim, A. Majumdar, *J. Heat Transfer* **2003**, *125*, 881.

[15] S. Lee, F. Yang, J. Suh, S. Yang, Y. Lee, G. Li, H. Sung Choe, A. Suslu, Y. Chen, C. Ko, J. Park, K. Liu, J. Li, K. Hippalgaonkar, J. J. Urban, S. Tongay, J. Wu, *Nat. Commun.* **2015**, *6*, 8573.

[16] I. Lutsyk, M. Rogala, P. Dabrowski, P. Krukowski, P. J. Kowalczyk, A. Busiakiewicz, D. A. Kowalczyk, E. Lacinska, J. Binder, N. Olszowska, M. Kopciuszynski, K. Szalowski, M. Gmitra, R. Stepniewski, M. Jalochowski, J. J. Kolodziej, A. Wysmolek, Z. Klusek, *Phys. Rev. B* **2018**, *98*, 195425.

[17] R. Inada, Y. Ōnuki, S. Tanuma, *Phys. Lett. A* **1979**, *69*, 453.

[18] M. D. Núñez-Regueiro, J. M. Lopez-Castillo, C. Ayache, *Phys. Rev. Lett.* **1985**, *55*, 1931.

[19] J. B. Balaguru Rayappan, S. A. C. Raj, N. Lawrence, *Physica B* **2010**, *405*, 3172.

[20] J. A. Benda, *Phys. Rev. B* **1974**, *10*, 1409.

[21] L. Lindsay, D. A. Broido, T. L. Reinecke, *Phys. Rev. Lett.* **2013**, *111*, 025901.

[22] F. Tian, B. Song, X. Chen, N. K. Ravichandran, Y. Lv, K. Chen, S. Sullivan, J. Kim, Y. Zhou, T.-H. Liu, M. Goni, Z. Ding, J. Sun, G. A. G. U. Gamage, H. Sun, H. Ziyaee, S. Huyan, L. Deng, J. Zhou, A. J. Schmidt, S. Chen, C.-W. Chu, P. Y. Huang, D. Broido, L. Shi, G. Chen, Z. Ren, *Science* **2018**, *361*, 582.

[23] J. S. Kang, M. Li, H. Wu, H. Nguyen, Y. Hu, *Science* **2018**, *361*, 575.

[24] S. Li, Q. Zheng, Y. Lv, X. Liu, X. Wang, P. Y. Huang, D. G. Cahill, B. Lv, *Science* **2018**, *361*, 579.

[25] D. A. Broido, T. L. Reinecke, *Phys. Rev. B* **2004**, *70*, 081310.

[26] K. Rossnagel, *J. Phys.: Condens. Matter* **2011**, *23*, 213001.

[27] K. R. A. Ziebeck, B. Dorner, W. G. Stirling, R. Schollhorn, *J. Phys. F: Met. Phys.* **1977**, *7*, 1139.

[28] M. Nakano, K. Shibuya, D. Okuyama, T. Hatano, S. Ono, M. Kawasaki, Y. Iwasa, Y. Tokura, *Nature* **2012**, *487*, 459.

[29] G. Wehmeyer, T. Yabuki, C. Monachon, J. Wu, C. Dames, *Appl. Phys. Rev.* **2017**, *4*, 041304.

[30] J. A. Tomko, A. Pena-Francesch, H. Jung, M. Tyagi, B. D. Allen, M. C. Demirel, P. E. Hopkins, *Nat. Nanotechnol.* **2018**, *13*, 959.

[31] K. T. Law, P. A. Lee, *Proc. Natl. Acad. Sci. USA* **2017**, *114*, 6996.

[32] B. C. Sales, O. Delaire, M. A. McGuire, A. F. May, *Phys. Rev. B* **2011**, *83*, 125209.

[33] J. W. Park, G. Y. Cho, J. Lee, H. W. Yeom, *Nat. Commun.* **2019**, *10*, 4038.

[34] H. Liu, H. S. Choe, Y. Chen, J. Suh, C. Ko, S. Tongay, J. Wu, *Appl. Phys. Lett.* **2017**, *111*, 102101.

[35] S. Lee, K. Hippalgaonkar, F. Yang, J. Hong, C. Ko, J. Suh, K. Liu, K. Wang, J. J. Urban, X. Zhang, C. Dames, S. A. Hartnoll, O. Delaire, J. Wu, *Science* **2017**, *355*, 371.

[36] J. Zhu, K. Hippalgaonkar, S. Shen, K. Wang, Y. Abate, S. Lee, J. Wu, X. Yin, A. Majumdar, X. Zhang, *Nano Lett.* **2014**, *14*, 4867.

[37] T. S. Toellner, A. Alatas, A. H. Said, *J. Synchrotron Radiat.* **2011**, *18*, 605.

[38] A. Alatas, A. H. Said, H. Sinn, G. Bortel, M. Y. Hu, J. Zhao, C. A. Burns, E. Burkel, E. E. Alp, *Phys. Rev. B* **2008**, *77*, 064301.

[39] F. Weber, R. Hott, R. Heid, K.-P. Bohnen, S. Rosenkranz, J.-P. Castellan, R. Osborn, A. H. Said, B. M. Leu, D. Reznik, *Phys. Rev. B* **2013**, *87*, 245111.

[40] G. Shirane, S. M. Shapiro, J. M. Tranquada, *Neutron Scattering with a Triple-Axis Spectrometer: Basic Techniques*, Cambridge University Press, Cambridge **2002**.

[41] J. D. Budai, J. Hong, M. E. Manley, E. D. Specht, C. W. Li, J. Z. Tischler, D. L. Abernathy, A. H. Said, B. M. Leu, L. A. Boatner, R. J. McQueeney, O. Delaire, *Nature* **2014**, *515*, 535.

[42] P. Giannozzi, S. Baroni, N. Bonini, M. Calandra, R. Car, C. Cavazzoni, D. Ceresoli, G. L. Chiarotti, M. Cococcioni, I. Dabo, A. D. Corso, S. D. Gironcoli, S. Fabris, G. Fratesi, R. Gebauer, U. Gerstmann, C. Gougoussis, A. Kokalj, M. Lazzeri, L. Martin-Samos, N. Marzari, F. Mauri, R. Mazzarello, S. Paolini, A. Pasquarello, L. Paulatto, C. Sbraccia, S. Scandolo, G. Sclauzero, A. P. Seitsonen, A. Smogunov, P. Umari, R. M. Wentzcovitch, *J. Phys.: Condens. Matter* **2009**, *21*, 395502.

[43] P. Giannozzi, O. Andreussi, T. Brumme, O. Bunau, M. B. Nardelli, M. Calandra, R. Car, C. Cavazzoni, D. Ceresoli, M. Cococcioni, N. Colonna, I. Carnimeo, A. D. Corso, S. D. Gironcoli, P. Delugas, R. A. DiStasio, A. Ferretti, A. Floris, G. Fratesi, G. Fugallo, R. Gebauer, U. Gerstmann, F. Giustino, T. Gorni, J. Jia, M. Kawamura, H.-Y. Ko, A. Kokalj, E. Küçükbenli, M. Lazzeri, M. Marsili, N. Marzari, F. Mauri, N. L. Nguyen, H.-V. Nguyen, A. Otero-de-la-Roza, L. Paulatto, S. Poncé, D. Rocca, R. Sabatini, B. Santra, M. Schlipf, A. P. Seitsonen, A. Smogunov, I. Timrov, T. Thonhauser, P. Umari, N. Vast, X. Wu, S. Baroni, *J. Phys.: Condens. Matter* **2017**, *29*, 465901.

[44] D. R. Hamann, *Phys. Rev. B* **2013**, *88*, 085117.

[45] S. Grimme, J. Antony, S. Ehrlich, H. Krieg, *J. Chem. Phys.* **2010**, *132*, 154104.

[46] Y. Liu, R. Ang, W. J. Lu, W. H. Song, L. J. Li, Y. P. Sun, *Appl. Phys. Lett.* **2013**, *102*, 192602.

[47] A. A. Mostofi, J. R. Yates, G. Pizzi, Y.-S. Lee, I. Souza, D. Vanderbilt, N. Marzari, *Comput. Phys. Commun.* **2014**, *185*, 2309.

[48] A. Kokalj, *Comput. Mater. Sci.* **2003**, *28*, 155.

[49] N. F. Hinsche, K. S. Thygesen, *2D Mater.* **2017**, *5*, 015009.

[50] D. L. Duong, M. Burghard, J. C. Schön, *Phys. Rev. B* **2015**, *92*, 245131.

[51] F. Giustino, M. L. Cohen, S. G. Louie, *Phys. Rev. B* **2007**, *76*, 165108.

[52] J. Noffsinger, F. Giustino, B. D. Malone, C.-H. Park, S. G. Louie, M. L. Cohen, *Comput. Phys. Commun.* **2010**, *181*, 2140.

[53] S. Poncé, E. R. Margine, C. Verdi, F. Giustino, *Comput. Phys. Commun.* **2016**, *209*, 116.

[54] M. Lazzeri, S. de Gironcoli, *Phys. Rev. Lett.* **1998**, *81*, 2096.

[55] L. Paulatto, F. Mauri, M. Lazzeri, *Phys. Rev. B* **2013**, *87*, 214303.

[56] G. Fugallo, M. Lazzeri, L. Paulatto, F. Mauri, *Phys. Rev. B* **2013**, *88*, 045430.

Supporting Information

Anomalously Suppressed Thermal Conduction by Electron-Phonon Coupling in Charge-Density-Wave Tantalum Disulfide

Huili Liu, Chao Yang, Bin Wei, Lei Jin, Ahmet Alatas, Ayman Said, Sefaattin Tongay, Fan Yang, Ali Javey, Jiawang Hong,* and Junqiao Wu*

1. Crystal structure and lattice parameters of normal phase 1T-TaS$_2$

Figure S7 shows the crystal structure of the normal phase of the octahedral (1T) polytype of TaS$_2$. Table S1 compares the lattice parameters from experimental data in literatures, as well as fully relaxed data in the simulation in this work. The lattice parameters theoretically calculated in this work are consistent with the experimental data in literature.

2. Lattice thermal conductivity of 1T-TaS$_2$: numerical fitting and discussion

In order to fit to the temperature dependence of lattice thermal conductivity ($\kappa_L(T)$), we use the Born-von Karman dispersion to approximate the acoustic phonon dispersion:[3, 4] $\omega = \omega_0 \sin(\pi q/2q_0)$, where ω_0 and q_0 depend on the mass, stiffness and lattice parameters of the crystal. Here $\omega_0 = 2\upsilon q_0/\pi$, where $q_0 = (6\pi^2\delta)^{1/3}$ is the Debye cutoff wavevector, υ is the acoustic phonon velocity in the long-wave limit, and δ is the number density of primitive unit cell.

We first fit to κ_L in the CCDW phase ($T < \sim 150$ K) using the Matthiessen's rule to combine different scattering mechanisms in the nanoribbons. The total phonon scattering rate is written as $1/\tau = 1/\tau_B + 1/\tau_I + 1/\tau_U$, where the three terms are for boundary (τ_B), impurity (τ_I) and ph-ph scattering (τ_U, Umklapp process), respectively. The frequency dependence of impurity scattering rate is expressed by the Rayleigh scattering model as $1/\tau_I = A\omega^4$, where A is a parameter related to defects concentration.[5] The general form of phonon-phonon

scattering rate is $1/\tau_U = B_1 \omega^2 T \exp(-B_2/T)$, where B_1 and B_2 are parameters related to bonding properties of the material.[6] The boundary scattering rate is expressed by $1/\tau_B = \upsilon/D_{eff}$, where D_{eff} is the effective sample size which is related to the particular shape and cross section area of the nanoribbons.[7] The surface are treated as diffusive. The fitting results are shown in Figure S8. The fitting yields $B_1 = 2.9 \times 10^{-18}$ s K^{-1} and $B_2 = 76$ K. The fitting yields a defects concentration that depends on the nanoribbon thickness, probably due to different extents of FIB damage and oxidization for nanoribbons with different thicknesses. The parameter A is 1.1×10^{-41} s^3, 1.7×10^{-41} s^3, 3.0×10^{-41} s^3 for 263 nm, 170 nm, 95 nm - thick nanoribbons, respectively. For comparison, in Figure S8 we also show the calculated κ_L of the CCDW phase of bulk TaS$_2$ by setting $D_{eff} = 1$ mm. Afterwards, an additional e-ph scattering term ($1/\tau_{e\text{-}ph}$) is incorporated into the Matthiessen's rule, to fit to the flat κ_L in the NCCDW phase (~150 K $< T < \sim350$ K). During this procedure, the same set of boundary, impurity scattering and Umklapp parameters are used for the given nanoribbon, as the sample is expected to retain the same geometry, purity and largely the same phonon-phonon scattering between the CCDW and NCCDW phases. Hence the total scattering rate is given by $1/\tau_{tot} = 1/\tau_D + 1/\tau_I + 1/\tau_U + 1/\tau_{e\text{-}ph}$. The additional term is $1/\tau_{e\text{-}ph} = C_1/T^{3/2}\exp(-\upsilon^2 C_2/T)\omega/\upsilon$, where C_1, C_2 are parameters related to the mass density, deformation potential, and carrier concentration at the Fermi level.[8] The parameters for the e-ph scattering were obtained from the fitting as C_1 $=2.9 \times 10^4$ m s^{-1} K$^{3/2}$, 3.9×10^4 m s^{-1} K$^{3/2}$, 2.8×10^4 m s^{-1} K$^{3/2}$ for 263 nm, 170 nm, 95 nm - thick nanoribbons, respectively. Therefore, the CCDW phase serves as a good reference to calibrate the ph-ph and e-ph scattering parameters in the NCCDW phase. All of these fitting parameters are tabulated in Table S2. The fitted curves are shown in Figure S8, which appropriately explain the nearly T-independent κ_L.

As discussed in the main text, κ_L is dominantly limited by strong e-ph scattering in the NCCDW phase, whereas ph-ph scattering is relatively weak. To highlight the unusually weak

ph-ph scattering in 1T-TaS$_2$, we compare it with 1T-HfS$_2$ which has very similar atomic masses and lattice structure. Unlike TaS$_2$, however, in HfS$_2$ the a-o bandgap diminishes, and its acoustic phonon dispersions are much less bunched,[9] providing large phase space for both the *aao* and *aaa* processes. This leads to strong ph-ph scattering and lower κ_L in bulk 1T-HfS$_2$. There is no experimental data reported on κ_L of 1T-HfS$_2$. Figure S9 shows the comparison of κ_L of 263nm thick TaS$_2$ nanoribbon (this work, experimental), bulk TaS$_2$ (experimental),[10] bulk TaS$_2$ (simulated, $D_{eff} = 1$ mm), bulk HfS$_2$ (calculated),[11] and monolayer HfS$_2$ (calculated).[12] Bulk TaS$_2$ in the CCDW phase ($T < \sim 150$ K) and monolayer HfS$_2$ both show the typical $\kappa_L \sim 1/T$ behavior as expected from dominant ph-ph scattering. However, the fact that the extrapolated κ_L value (black dashed line) of bulk TaS$_2$ is higher than that of bulk HfS$_2$ (red point) at 300 K is an indication of weaker ph-ph scattering in TaS$_2$, considering the higher sound velocity and nearly equal specific heat in HfS$_2$ (Table S3). Considering that experimental thermal conductivity is typically lower than theoretical value due to impurity and boundary scattering, the real difference in κ_L between TaS$_2$ and HfS$_2$ might be even larger. The comparison of parameters between 1T-TaS$_2$ and 1T-HfS$_2$ is tabulated in Table S3.

It is intriguing to look at the lattice thermal resistivity ($1/\kappa_L$) of 1T-TaS$_2$, as shown in Figure S10. The jump in $1/\kappa_L$ between the CCDW and NCCDW phase are nearly constant (~ 0.17 m K W^{-1}) for these nanoribbons. They are independent of the nanoribbon thickness. If the thermal resistivity is approximately written as $1/\kappa_L = 1/\kappa_B + 1/\kappa_I + 1/\kappa_U + 1/\kappa_{\text{e-ph}}$, where each term represents the thermal resistivity arising from boundary, impurity, ph-ph, and e-ph scattering, the jump in $1/\kappa_L$ between the CCDW and NCCDW phases could be mainly attributed to the e-ph scattering emerging in NCCDW phase.

3. Phonon dispersion and phonon linewidth in the ICCDW phase

We also collected data of the phonon dispersion and phonon linewidth in the ICCDW phase at 450 K, as shown in Figure S11 and Supplementary Figure S12, respectively. The phonon dispersion shows very similar acoustic phonons compared to the NCCDW phase. The energy of these phonons is consistent with theoretical prediction based on the normal phase (solid line).

4. Comparison of experimental acoustic phonon branches between inelastic X-ray scattering (IXS) and neutron scattering measurements

We compared the acoustic phonon dispersions measured in this work with neutron scattering measurements.[16] Because of lack of data of full phonon branches in the literature, we show in Figure S13 the acoustic phonon branches along the Γ-M direction. It is clear that the acoustic phonon dispersions in this work are consistent with that in the literature. Both measurements show a dip in the longitudinal acoustic (LA) phonon branch along the Γ-M direction, near the wavevector of approximately 0.6 $q_{\text{Γ-M}}$, indicating phonons mode softening as the Kohn anomaly.

References

[1]   G. Hagg, N. Schonberg, *Arkiv Kemi* **1954**, *Vol: 7, No. 4.*
[2]   Y. Liu, R. Ang, W. J. Lu, W. H. Song, L. J. Li, Y. P. Sun, *Appl. Phys. Lett.* **2013**, *102*, 192602.
[3]   N. W. Ashcroft, N. D. Mermin, *Solid State Physics*, Holt, Rinehart and Winston, New York **1976**.
[4]   C. Kittel, *Introduction to Solid State Physics*, Wiley, New York **1996**.
[5]   B. Abeles, *Phys. Rev.* **1963**, *131*, 1906.
[6]   Y. J. Han, P. G. Klemens, *Phys. Rev. B* **1993**, *48*, 6033.
[7]   A. K. McCurdy, H. J. Maris, C. Elbaum, *Phys. Rev. B* **1970**, *2*, 4077.
[8]   B. Liao, B. Qiu, J. Zhou, S. Huberman, K. Esfarjani, G. Chen, *Phys. Rev. Lett.* **2015**, *114*, 115901.
[9]   G. Yumnam, T. Pandey, A. K. Singh, *J. Chem. Phys.* **2015**, *143*, 234704.
[10]   M. D. Núñez-Regueiro, J. M. Lopez-Castillo, C. Ayache, *Phys. Rev. Lett.* **1985**, *55*, 1931.
[11]   K. F. Garrity, *Phys. Rev. B* **2016**, *94*, 045122.
[12]   X. Gu, R. Yang, *Appl. Phys. Lett.* **2014**, *105*, 131903.
[13]   J. A. Benda, *Phys. Rev. B* **1974**, *10*, 1409.
[14]   H. P. B. Rimmington, A. A. Balchin, *J. Mater. Sci.* **1974**, *9*, 343.
[15]   I. Lutsyk, M. Rogala, P. Dabrowski, P. Krukowski, P. J. Kowalczyk, A. Busiakiewicz, D. A. Kowalczyk, E. Lacinska, J. Binder, N. Olszowska, M. Kopciuszynski, K. Szalowski, M.

Gmitra, R. Stepniewski, M. Jalochowski, J. J. Kolodziej, A. Wysmolek, Z. Klusek, *Phys. Rev. B* **2018**, *98*, 195425.

[16]   K. R. A. Ziebeck, B. Dorner, W. G. Stirling, R. Schollhorn, *J. Phys. F: Met. Phys.* **1977**, *7*, 1139.
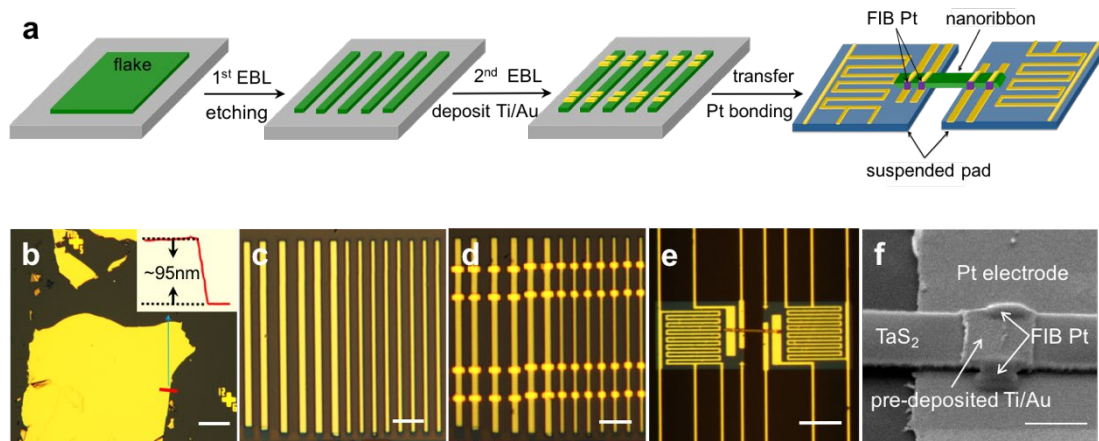
Figure S1. 1T-TaS$_2$ nanoribbons device fabrication. a) Schematic representation of the TaS$_2$ nanoribbon fabrication process. Optical images of the flake (b), nanoribbons (c, d), and device (e). Inset in (b) shows the thickness of the flake measured along the red line by an AFM. f) A SEM image of the nanoribbon that was FIB-bonded onto the underlying Pt electrode. Scale bar: 50 μm (b), 5 μm (c, d), 20 μm (e), 1 μm (f).
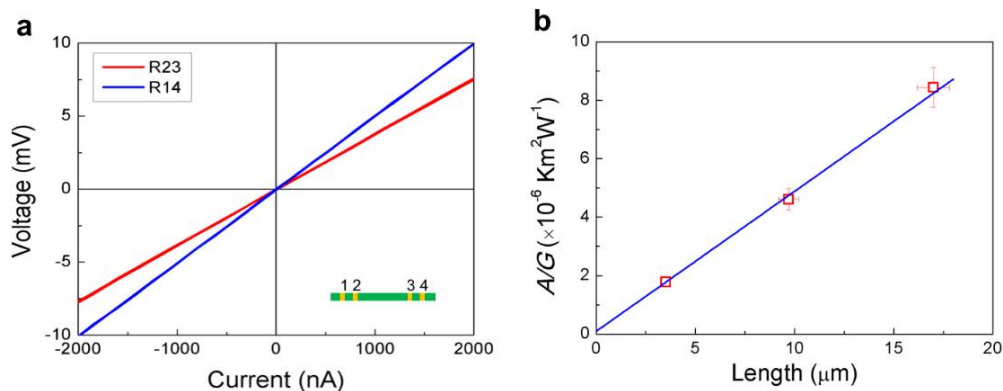
Figure S2. a) Linear I-V relationship of the nanoribbons based on a two-probe measurement, indicating an electrical ohmic contact between the nanoribbon and the electrodes. b) Plot of total thermal resistance (1/G) multiplied by cross-sectional area (A) as a function of the nanoribbon length (measured at 300K), indicating that the thermal contact resistance between the nanoribbon and pads is negligible. Error bars include errors ~8% for A/G and ~5% for the nanoribbon length from thermal conductance and dimension measurements of nanoribbons, respectively.
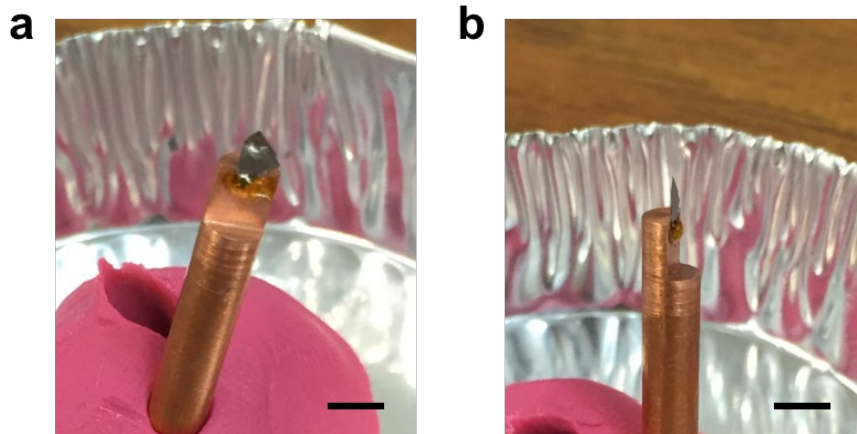
Figure S3. Optical image of a 1T-TaS$_2$ single crystal flake mounted on the copper rod. The single crystal flake has a lateral size of 2 ~ 3 mm and a thickness of 50 ~ 100 μm for the inelastic X-ray scattering measurements. Scale bar: 5 mm (a), (b).
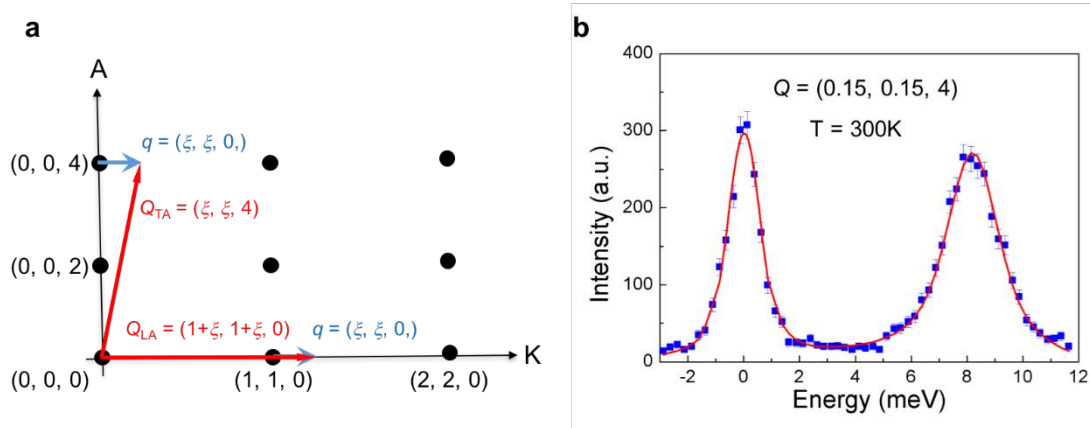

Figure S4. IXS measurements for individual phonon branch. A schematic representation of IXS measurements for individual phonon branches. a) Total scattering vectors, Q_{LA} and Q_{TA}, for separate measurements of longitudinal and transverse phonons with wavevector $q = (\xi, \xi, 0)$ along the Γ-K symmetry direction. b) Plot of the experimental energy scan at $Q = (0.15, 0.15, 4)$ in the transverse acoustic branch at 300 K. The line-shape is well fitted by the damped harmonic oscillator model for the inelastic peak and a Gaussian function for the elastic peak.
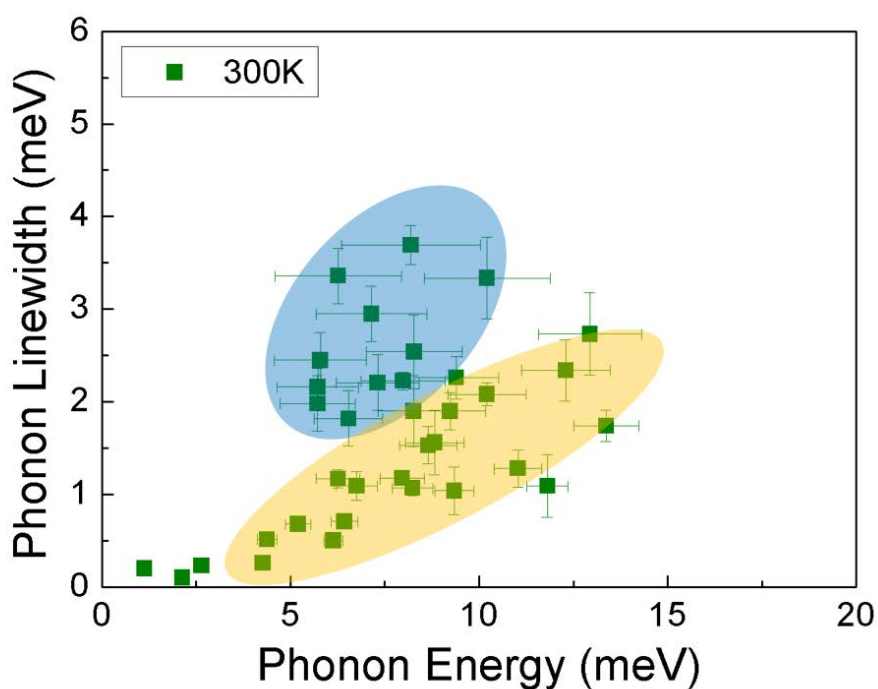
Figure S5. Phonon linewidth versus phonon energy at 300 K. Phonon linewidth for dispersive (yellow ellipse) and less-dispersive (blue ellipse) phonon modes in NCCDW phase. The linewidth was extracted from the Inelastic X-Ray Scattering measurements. For the less-dispersive phonon modes in the range of 5~10 meV, the phonon linewidths are unusually broadened from those of the dispersive modes. In the NCCDW phase of 1T-TaS$_2$, the lattice vibration is strongly damped at these less-dispersive phonon modes, which is attributed to the strong e-ph interaction mediated by the Fermi surface nesting.
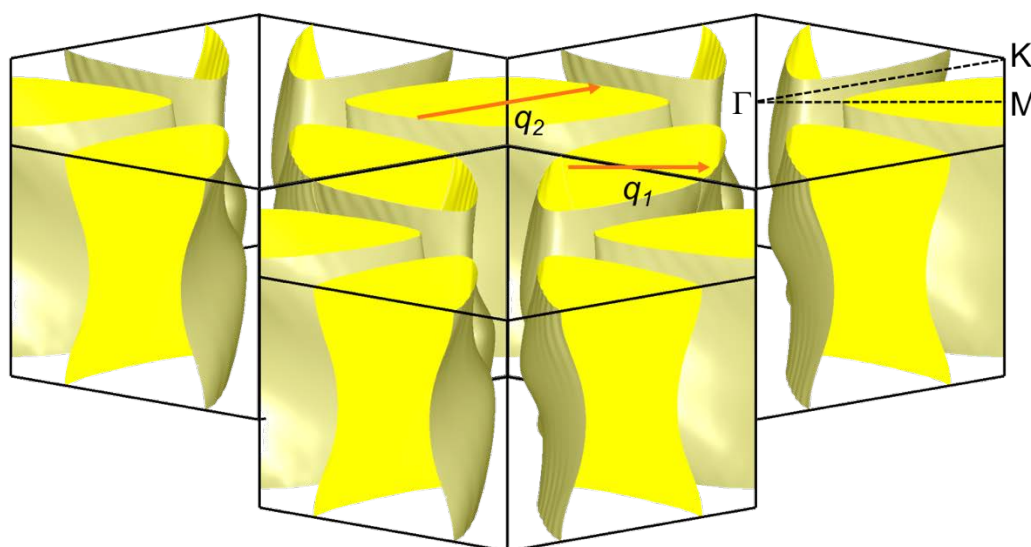

Figure S6. Calculated Fermi surface (3D) of 1T-TaS$_2$ in the normal phase. This shows, in three-dimensional view, that the Fermi surface is nested with the two electron wavevectors q_1, and q_2 along the Γ-M and Γ-K directions, respectively.
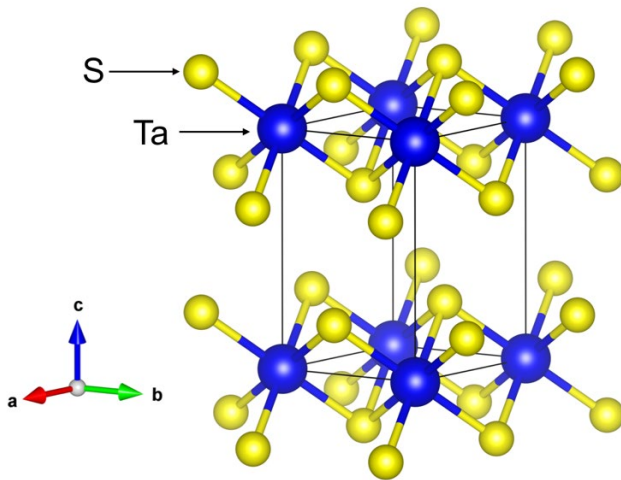
7

Figure S7. Crystal structure of normal phase 1T-TaS$_2$.
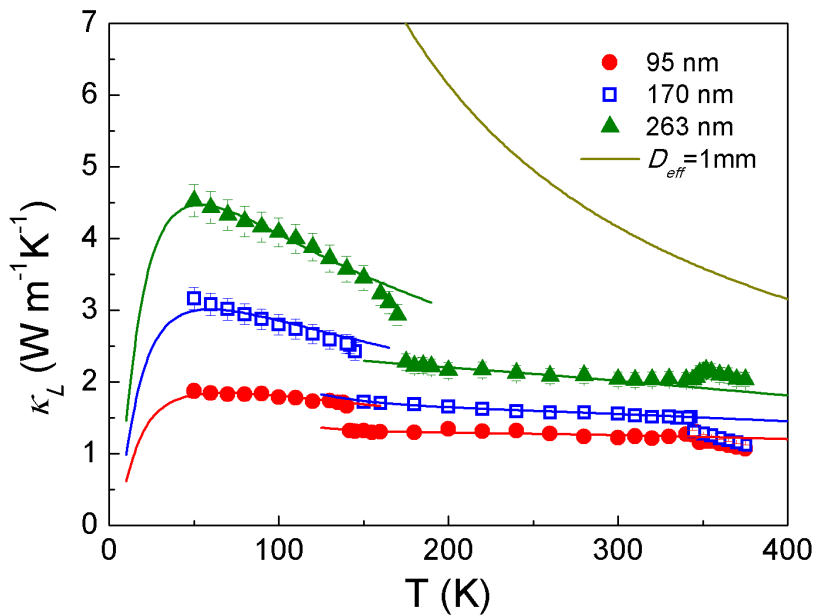
Figure S8. Lattice thermal conductivity (κ_L) obtained by subtracting electron contribution (κ_e) from measured κ assuming the Wiedemann-Franz law ($\kappa_e = L_0\sigma T$). Lines are fitting using total scattering rate of $1/\tau = 1/\tau_B + 1/\tau_I + 1/\tau_U$ for the CCDW phase and $1/\tau = 1/\tau_B + 1/\tau_I + 1/\tau_U + 1/\tau_{e\text{-}ph}$ for the NCCDW phase. As a comparison, we also plotted κ_L simulated for bulk TaS$_2$ (using $D_{eff} = 1$ mm), following the simulation model and parameters used for the CCDW phase.
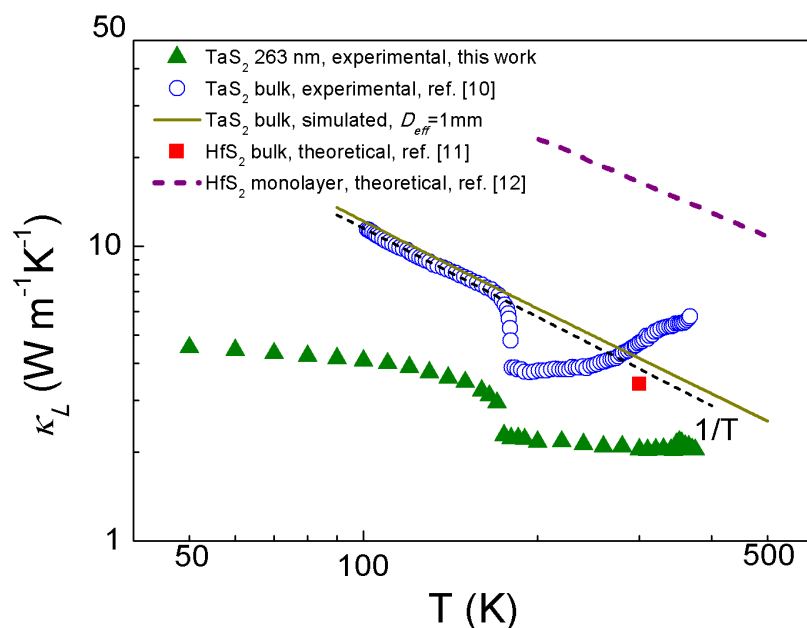
Figure S9. Comparison of lattice thermal conductivity of 1T-TaS$_2$ and 1T-HfS$_2$. Black dashed line indicates the typical 1/T-dependence of κ_L in the CCDW phase of bulk TaS$_2$ limited by phonon-phonon scattering.
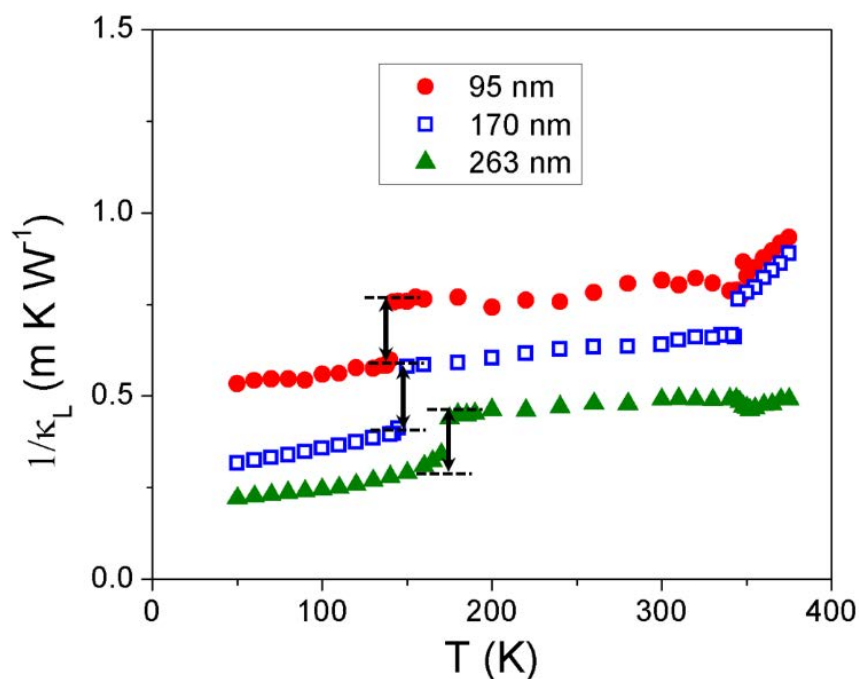

Figure S10. Temperature dependence of the lattice thermal resistivity ($1/\kappa_L$). Nearly the same amount of reduction in $1/\kappa_L$ going from the CCDW to the NCCDW phase was observed for nanoribbons with different thicknesses. The total scattering rate is $1/\tau_{tot} = 1/\tau_0 + 1/\tau_{e\text{-}ph}$, where $1/\tau_0 = 1/\tau_B + 1/\tau_I + 1/\tau_U$. The total lattice thermal resistivity is approximately expressed by

$1/\kappa_L = 1/\kappa_0 + 1/\kappa_{e\text{-}ph}$, hence the amount of jump in $1/\kappa_L$ in this figure is attributed mostly to e-ph coupling, which is ~ 0.17 m-K W^{-1} as indicated by black arrows.
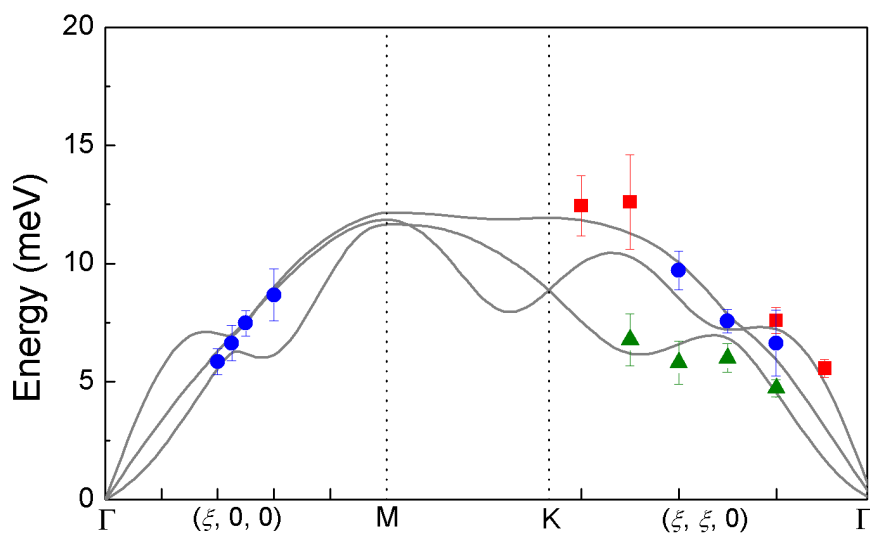

Figure S11. Acoustic phonon dispersion of the ICCDW phase measured at 450K by inelastic X-ray scattering (IXS), overlaid onto the calculated dispersion. The measured phonon linewidth is represented by the error bars.
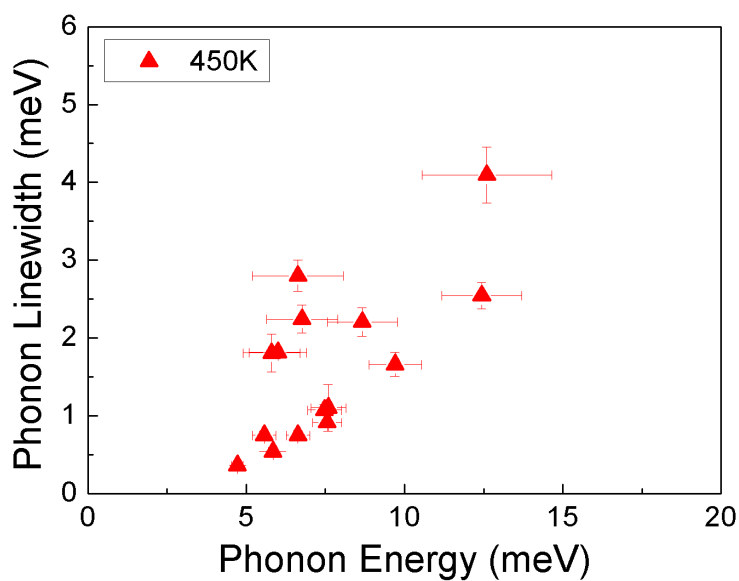

Figure S12. Phonon linewidth versus phonon energy for the ICCDW phase of 1T-TaS$_2$ at 450K.
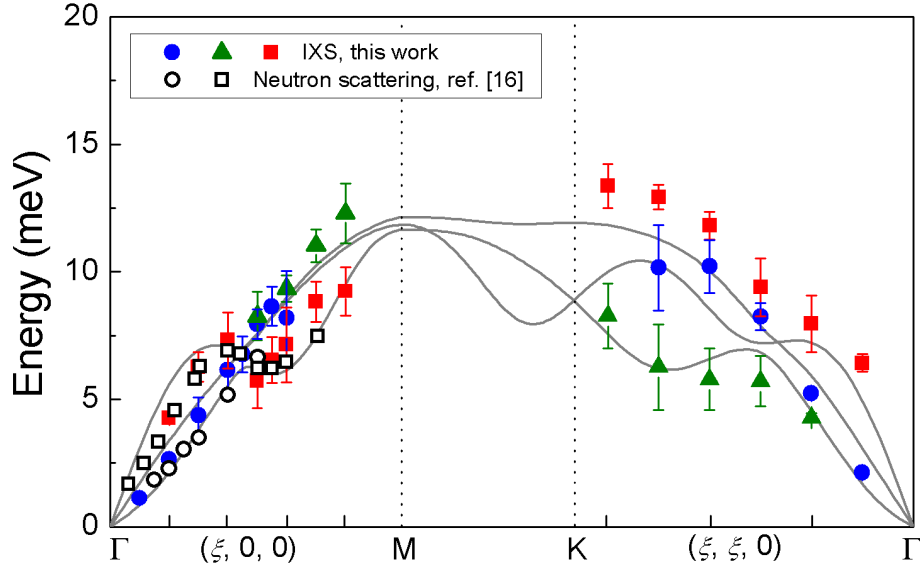
Figure S13. Comparison of phonon dispersions obtained from inelastic X-ray scattering (IXS) and from neutron scattering measurements. Solid points are from IXS measurements, and open points are extracted from the literature (ref. [16]) of neutron scattering measurements.

Table S1. Experimental and calculated lattice parameters of 1T-TaS$_2$.

	Experimetal[1]	Experimental[2]	Calculated (this work)
Space group		P$\bar{3}$m1 (164)	
Z		1	
a (Å)	3.350	3.367	3.350
b (Å)	3.350	3.367	3.350
c (Å)	5.860	5.902	5.954
α		90^0	
β		90^0	
γ		120^0	
Volume (Å^3)	56.953	57.955	57.867

Table S2. Parameters obtained from κ_L(T) fitting in the CCDW and NCCDW phases of 1T-TaS$_2$.

Nanoribbons		Device 1	Device 2	Device 3
	Lattice parameters	$a = b = 3.350$ Å, $c = 5.954$ Å, $\alpha = \beta = 90^0$, $\gamma = 120^0$		
	Debye temperature θ_D (K)	172 [13]		
	Thickness (nm)	95	170	263
	Width (μm)	1.20	1.14	1.34
CCDW	D_{eff} (nm)	268	401	569
	B_1 (s K^{-1})	2.9×10^{-18}		
	B_2 (K)	76		
	A (s^3)	3.0×10^{-41}	1.7×10^{-41}	1.1×10^{-41}
NCCDW	D_{eff} (nm)	268	401	569
	B_1 (s K^{-1})	2.9×10^{-18}		
	B_2 (K)	76		
	A (s^3)	3.0×10^{-41}	1.7×10^{-41}	1.1×10^{-41}
	C_1 (m s^{-1} K$^{3/2}$)	2.8×10^4	3.9×10^4	2.9×10^4
	C_2 (s^2 K m^{-2})	4.2×10^{-5}		

Table S3. Comparison of physical parameters and properties between 1T-TaS$_2$ and 1T-HfS$_2$.

	1T-TaS$_2$	1T-HfS$_2$
Space group	P$\bar{3}$m1 (164)	P$\bar{3}$m1 (164)
Lattice parameters	$a = b = 3.350$ Å, $c = 5.954$ Å, $\alpha = \beta = 90^0$, $\gamma = 120^0$	$a = b = 3.623$ Å, $c = 5.841$ Å, $\alpha = \beta = 90^0$, $\gamma = 120^0$ [14]
Atomic masses	Ta/S = 181/32	Hf/S = 178/32

Debye temperature θ_D (K)	172 [13]	289.5 [11]
$\hbar\omega_{min}^{optical}$ (meV)	26.5	16.9 [9]
$\hbar\omega_{max}^{acoustic}$ (meV)	11.6	17.7 [9]
a-o gap ratio, $(\hbar\omega_{min}^{optical} - \hbar\omega_{max}^{acoustic})/\hbar\omega_{max}^{acoustic}$	~ 1.3	~ 0
Specific heat capacity (J mol^{-1} K^{-1}, 300K)	23.6	23.7
Speed of sound (m s^{-1})	2235	3935
κ_L (bulk, 300 K, W m^{-1} K^{-1})	~ 4.7 [10] (experimental)	3.4 [11] (theoretical)
Band gap (eV)	metallic (300 K) [15]	1.6 [11]